


Please cite the Published Version

Yin, S, Chen, H, Chen, J, Massoudi, A, Deng, W, Gao, X, Zhang, S, Wang, Y, Lin, TW, Banks, CE , Qiao, SZ, Zou, G, Hou, H and Ji, X (2022) Chemical-mechanical effects in Ni-rich cathode materials. Chemistry of Materials, 34 (4). pp. 1509-1523. ISSN 0897-4756

DOI: <https://doi.org/10.1021/acs.chemmater.1c03051>

Publisher: American Chemical Society

Version: Accepted Version

Downloaded from: <https://e-space.mmu.ac.uk/631350/>

Usage rights:  In Copyright

Additional Information: This document is the Accepted Manuscript version of a Published Work that appeared in final form in Chemistry of Materials, copyright © American Chemical Society after peer review and technical editing by the publisher. To access the final edited and published work see <https://doi.org/10.1021/acs.chemmater.1c03051>.

Enquiries:

If you have questions about this document, contact openresearch@mmu.ac.uk. Please include the URL of the record in e-space. If you believe that your, or a third party's rights have been compromised through this document please see our Take Down policy (available from <https://www.mmu.ac.uk/library/using-the-library/policies-and-guidelines>)

Chemical-Mechanical Effects in Ni-Rich Cathode Materials

Shouyi Yin, Hongyi Chen, Jun Chen, Abouzar Massoudi, Wentao Deng, Xu Gao, Shu Zhang, Ying Wang, Tsung-Wu Lin, Craig E. Banks, Shi-zhang Qiao, Guoqiang Zou, Hongshuai Hou, Hongshuai Hou and Xiaobo J*

Correspondence: Email: xji@csu.edu.cn

Author details:

Shouyi Yin - State Key Laboratory of Powder Metallurgy, College of Chemistry and Chemical Engineering, Central South University, Changsha 410083, China

Hongyi Chen - State Key Laboratory of Powder Metallurgy, College of Chemistry and Chemical Engineering, Central South University, Changsha 410083, China

Jun Chen - State Key Laboratory of Powder Metallurgy, College of Chemistry and Chemical Engineering, Central South University, Changsha 410083, China

Abouzar Massoudi - Department Nanotechnology and Advanced Materials, Materials and Energy Research Center (MERC), P.O. Box, Tehran 14155-4777, Iran;

Wentao Deng - State Key Laboratory of Powder Metallurgy, College of Chemistry and Chemical Engineering, Central South University, Changsha 410083, China

Xu Gao - State Key Laboratory of Powder Metallurgy, College of Chemistry and Chemical Engineering, Central South University, Changsha 410083, China

Shu Zhang - State Key Laboratory of Powder Metallurgy, College of Chemistry and Chemical Engineering, Central South University, Changsha 410083, China

Ying Wang - Department of Chemistry, The Chinese University of Hong Kong, Shatin, New Territories, Hong Kong 999077, China;

Tsung-Wu Lin - Department of Chemistry, Tunghai University, No. 1727, Sec. 4, Taiwan Boulevard Xitun District, Taichung 40704, Taiwan;

Craig E. Banks - Manchester Fuel Cell Innovation Centre, Faculty of Science and Engineering, Manchester Metropolitan University, Chester Street, Manchester M1 5GD, U.K.;

Shi-zhang Qiao - School of Chemical Engineering, The University of Adelaide, Adelaide, South Australia 5005 Australia;

Guoqiang Zou - State Key Laboratory of Powder Metallurgy, College of Chemistry and Chemical Engineering, Central South University, Changsha 410083, China

Hongshuai Hou – State Key Laboratory of Powder Metallurgy, College of Chemistry and Chemical Engineering, Central South University, Changsha 410083, China;

Xiaobo Ji - State Key Laboratory of Powder Metallurgy, College of Chemistry and Chemical Engineering, Central South University, Changsha 410083, China;

Abstract

The implementation of Ni-rich cathodes with high energy density has been critically restrained by stress corrosion. Herein, crack-free LiNbO_3 -coated $\text{LiNi}_{0.88}\text{Co}_{0.10}\text{Mn}_{0.02}\text{O}_2$, as theoretically predicted, demonstrates highly reversible lithiation/delithiation. Mechanically, the phase transition ($\text{H1} \rightarrow \text{H2} \rightarrow \text{H3}$) is significantly alleviated by the excogitation of the interfacial force invoked by the LiNbO_3 coating layer, as verified by X-ray absorption spectroscopy and extended X-ray absorption near-edge structure spectroscopy. Meanwhile, the stabilities of the crystal structure are remarkably strengthened by the strong Nb–O bond activated by Nb^{5+} doping that is confirmed by Rietveld refinement of X-ray diffraction and differential capacitance curves. Chemically, the interface shielding effect is conducive to protecting the electrode against electrolyte corrosion along with subsequent transition-metal dissolution, ultimately rendering a faster/highly convertible lithium-ion diffusion. Greatly, the excellent electrochemical properties (74% capacity retention after 300 cycles at 2 C within 2.5–4.3 V) and structural stability (the morphology remains intact after 500 cycles at 5 C within 2.5–4.3 V) are successfully achieved. Given this, this elaborate work might inaugurate a potential avenue for rationally tuning the structure/interface evolution toward Ni-rich materials.

Introduction

Future cathode materials of lithium-ion batteries require a higher energy density, stronger cycle stability, and more safety performance to meet the increased demands of consumers. (1–6) Ni-rich cathodes, such as $\text{Li}[\text{Ni}_x\text{Co}_y\text{Mn}_{1-x-y}]\text{O}_2$ (NCM) and $\text{Li}[\text{Ni}_x\text{Co}_y\text{Al}_{1-x-y}]\text{O}_2$ (NCA) (x is more than 0.8), are excellent in providing a high energy density, but their stability is relatively poor. (7–9) In fact, the low stability of Ni-rich cathodes results from the structure collapse after cycling, which is mainly caused by stress corrosion cracking (SCC). (10) It was proposed that this SCC problem could be attributed to the anisotropic change in lattice parameters, where the stress concentration inside the secondary particles comes from their $\text{H}_2 \rightarrow \text{H}_3$ phase transition during the charging and discharging processes. (9,11,12) In addition, heterogeneous charge/discharge kinetics behavior could accelerate the rupture of the particles. (13,14) Moreover, once the secondary particle is penetrated by the crack, it would be seriously invaded by the electrolyte, leading to irreversible side reactions with increased local impedance of the particles that affect the utilization of the particles. (14) Therefore, the SCC problem can also be summarized as a process of “chemical-mechanical failure”.

In order to improve the mechanical stability, crystal texture enhancement and lattice structure improvement are focused by many researchers, aiming to design a type of secondary particle without anisotropic stress concentration. (15,16) In addition, there are many research studies about single crystal particles because these kinds of materials have no grain boundaries, which means that they will be less affected by anisotropic lattice parameter changes and then achieve an excellent stability. (17) Moreover, chemical problems, such as the electrolyte erosion (the reaction of HF with tetravalent nickel) (18) and surface residual lithium (the surface pH value will be increased by Li_2CO_3 , LiOH), (19) leading to surface degradation, can be solved by designing stable metal oxide coating layers and lithium compounds. Furthermore, it was found that this improved coating would provide an interface with uniform lithium-ion distribution (lithium-ion conductors like Li_2TiO_3 , (20–22) LiAlO_2 , (20) LiZrO_3 , (23) Li_2SiO_3 , (24) and Li_3VO_4 (25)), (26) which can achieve a homogeneous phase diffusion on the particle surface, and then, the internal stress concentration level of secondary particles can be reduced. (14) Although many studies have investigated the methods to solve the SCC problem, there is not much about both chemical and mechanical enhancement. The relationships of chemical and mechanical improvement need to be further studied, such as, the connection between the alleviation of $\text{H}_2 \rightarrow \text{H}_3$ phase transition, the uniformity of lithium-ion charge/discharge kinetics, and the elimination of cracks. As a result, we explored both the boost mechanisms simultaneously.

Hereby, LiNbO_3 (LNO) is employed to design a kind of crack-free Ni-rich cathode, which can achieve both the aspects at the same time, confirmed by the phase diagram (Figure 1g). Mechanically, by means of density functional theory (DFT) calculations, we investigate the mechanical effect of the force from the coating layer to suppress phase transitions. In addition, the Rietveld refinement of X-ray diffraction (XRD) and extended X-ray absorption fine structure (EXAFS) are employed to analyze the changes in the crystal structure and atomic bonds. Moreover, phase transitions and lithium-ion distribution uniformity are verified by X-ray absorption spectroscopy (XAS) and extended X-ray absorption near-edge structure (XANES) spectroscopy. Besides, from the chemical perspective, X-ray photoelectron spectroscopy (XPS) and electrochemical impedance spectroscopy (EIS) are used to study the surface chemical side reactions. Furthermore, the Arrhenius equation and galvanostatic intermittent titration technique (GITT) are regarded as tools for studying lithium-ion kinetics. Expectedly, with the assistance of the mechanics/chemistry coupling effect, excellent electrochemical performance and structural stability [proved by scanning electron microscopy (SEM)] are successfully achieved.

2. Results and Discussion

2.1. Proposed Crack-free Cathode Materials from Mechanical Perspectives

All Ni-rich cathodes undergo a series of phase transitions during charging: the original H1 phase is transformed into a monoclinic phase (M), subsequently converted into H2 and H3 phases as shown by the lattice parameter characterizations in Figure 1e. (9) This can trigger extremely adverse impacts on the stability of the Ni-rich cathode. (27) As a result, the most feasible way to improve structural stability is to hinder phase transition.

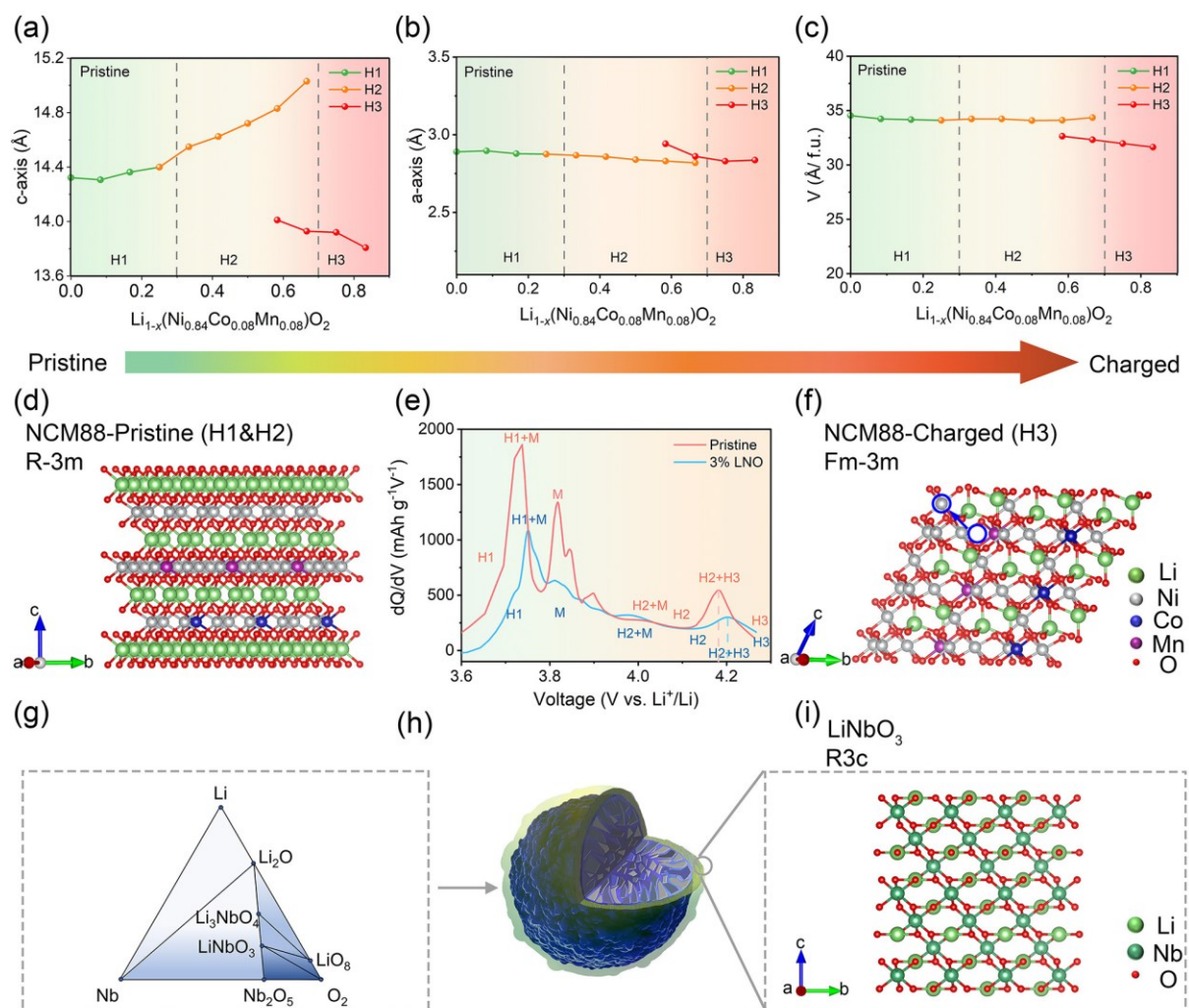


Figure 1. Lattice parameters of the (a) c-axis, (b) a-axis, and (c) unit cell volume calculated by DFT. Atomic structure model of (d) H1 → H2 and (f) H3 phases of NCM88. (e) Comparison of the differential capacitance curves. (g) Phase diagram of LiNbO3. (h,i) Structure of the designed material and the atomic structure of the coating layer.

To understand the mechanics of the phase transition, DFT calculations are performed to simulate the change in the lattice parameters of pristine NCM88 cathode during the charging process, as shown in Figure 1. In the H1 \rightarrow H2 phase transition process, the lattice parameter c-axis is increased to some extent, the a-axis is slightly decreased, and the lattice volume is expanded slightly. However, when it comes to the H3 phase, the lattice parameter c-axis is decreased suddenly, the a-axis still falls slowly, and the lattice volume is dropped similar to the c-axis lattice parameter. All these above results show that phase transition from H2 to H3 can bring a significant structural change, which might cause the cracks and worsen the electrochemical performances. (8,28)

Moreover, to explore the mechanism of lattice parameter changes, the O–O interaction in the interslab has been investigated by analyzing the different charge densities. The distance of the O atom layers is increased from $\text{Li}[\text{Ni}_{0.84}\text{Co}_{0.08}\text{Mn}_{0.08}]\text{O}_2$ to $\text{Li}_{0.25}[\text{Ni}_{0.84}\text{Co}_{0.08}\text{Mn}_{0.08}]\text{O}_2$ (in the H2 phase transition state) (see in Figure 2e,h), indicating the increase in the O–O repulsive force, which is further confirmed by the results of the DFT calculation (Figure 2a). As shown in Figure 2d,g, the value of $-\text{pCOOP}$, weighted by the overlap matrix elements, tends to be 0 after charging, which offers the information of less overlap of O atomic orbitals that refers to a strong repulsive force between those O atoms. It is the repulsive force that leads to the increase in lattice parameter at the c-axis during the processing of the H1 \rightarrow H2 phase transition. However, Ni atoms enter into the Li site within the H3 phase, which can reduce the O–O repulsive force. Subsequently, the increase in the c-axis is doped in relative to the change in the H1 \rightarrow H2 process. However, the collapse of the original layered structure leads to the formation of the H3 phase when the lithium ion is highly deficient (Figure 1f), bringing an abrupt decrease of c-axis lattice parameters with the as-generated H3 phase.

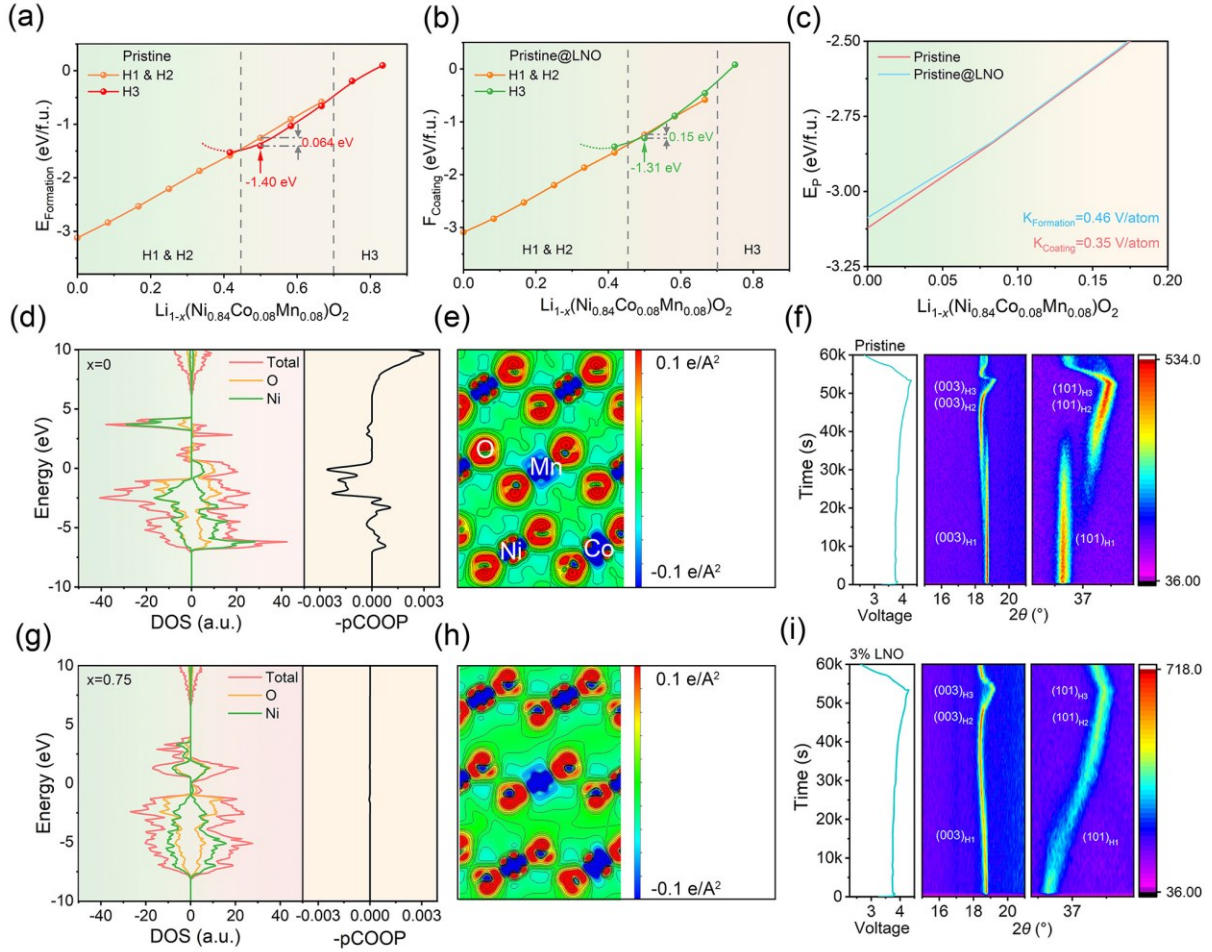


Figure 2. Comparison of the formation energies of H1 \rightarrow H2 and H3 phases between (a) blank group and (b) experimental group through DFT calculations. (c) Comparison of curvatures of H1 and H2 curves of the curve $E_{\text{Formation}}-x$ and $E_{\text{Coating}}-x$ in (a,b). Electronic density of states of (d) $\text{Li}_{1-x}(\text{Ni}_{0.84}\text{Co}_{0.08}\text{Mn}_{0.08})\text{O}_2$ ($x = 0$) and (g) $\text{Li}_{1-x}(\text{Ni}_{0.84}\text{Co}_{0.08}\text{Mn}_{0.08})\text{O}_2$ ($x \approx 0.75$). The differential charge density of (e) $\text{Li}_{1-x}(\text{Ni}_{0.84}\text{Co}_{0.08}\text{Mn}_{0.08})\text{O}_2$ ($x = 0$) and (h) $\text{Li}_{1-x}(\text{Ni}_{0.84}\text{Co}_{0.08}\text{Mn}_{0.08})\text{O}_2$ ($x \approx 0.75$). In situ XRD of the (f) pristine sample and (i) 3% LNO sample.

In summary, to reduce cracks and improve structural stability, it is imperative to suppress the changes of the above-mentioned lattice parameters, that is, the phase transition. It is eager to explore the mechanical effects of “coating” on secondary particles. Hence, a rigid material with good mechanical properties is suitable as a coating layer, which can allow researchers to investigate the influences of the force for the coating layer inside the cathode secondary particles. Compared with the Ni-rich cathode, LNO has good mechanical performances (Tables S9–S11, Supporting Information) and an excellent lithium-ion conductivity ($10^{-5} \text{ cm}^2 \text{ s}^{-1}$ at room temperature). Therefore, it is feasible to create an LNO-coated Ni-rich cathode. More importantly, the DFT calculation results reveal that LNO plays a

mechanical role in inhibiting phase transition because a protective force is provided by the coating layer whose mechanical properties are much stronger than those of NCM materials (Tables S9–S11, Supporting Information).

The formation energy of $\text{Li}_{1-x}[\text{Ni}_{0.84}\text{Co}_{0.08}\text{Mn}_{0.08}]\text{O}_2$ ($E_{\text{Formation}}$) and $\text{Li}_{1-x}[\text{Ni}_{0.84}\text{Co}_{0.08}\text{Mn}_{0.08}]\text{O}_2$ with LNO coating (E_{Coating}) is calculated, aiming to further understand the hindering effect of the coating layer on the degradation, (13) where $E_{\text{Formation}}$ is gained by

$$E_{\text{Formation}} = E_{\text{Li}_{1-x}\text{Ni}_{0.84}\text{Co}_{0.08}\text{Mn}_{0.08}\text{O}_2} - (1-x)E_{\text{Li}} - 0.84E_{\text{Ni}} - 0.08E_{\text{Co}} - 0.08E_{\text{Mn}} - 2E_{\text{O}} \quad (2.1)$$

where $E_{\text{Li}_{1-x}\text{Ni}_{0.84}\text{Co}_{0.08}\text{Mn}_{0.08}\text{O}_2}$ means the total energy when x number of Li^+ is removed during the charging process, and E_{Li} , E_{Ni} , E_{Co} , E_{Mn} , and E_{O} are the total energies of the Li, Ni, Co, Mn, and O elements, respectively. The calculated results show that the delithiation voltage of the pristine NCM88 cathode is 3.759 V (the slope of the H1 and H2 curves in Figure 2a), which is well consistent with the experimental results (3.737 V as shown in Figure 1e). For the phase transition from the H1 phase to the H2 phase, the curve of $E_{\text{Formation}-x}$ is almost a straight line (see Figure 2a). Thus, a low energy barrier for the pure $\text{Li}_{1-x}[\text{Ni}_{0.84}\text{Co}_{0.08}\text{Mn}_{0.08}]\text{O}_2$ phase decomposed to the binary phase (H1 and H2) will cause the coexistence of the H1 and H2 phases, corresponding to a split of the (003) plane at 20–30 ks in the in situ XRD (in situ XRD) pattern (Figure 1f). The slope of the x -curve shows that a potential of 4.506 V is required for complete conversion from the H1 phase to the H3 phase (Figure 1a). When $x > 0.5$, the $E_{\text{Formation}}$ of the H3 phase is significantly lower than that of the H2 phase. It reveals that the H2 phase can be easily transferred to the H3 phase after delithiation over 50%.

Furthermore, the E_{Coating} is as follows: (29)

$$E_{\text{Coating}} = E_{\text{Formation}} - \frac{2}{3}G \left(\frac{\delta V}{V_{\text{initial}}} \right)^2 V_{\text{f.u.}} \quad (2.2)$$

where G is the shear modulus of LNO and V_{initial} is the volume of the NCM88 particle before the charging process; δV is the increased volume of the NCM88 particle during the delithiation, and $\delta V/V_{\text{initial}}$ can be estimated by Figure S1 (Supporting Information). $V_{\text{f.u.}}$ is the volume of NCM88 per formula unit. The second term of eq 2.2 is referred to the strain energy caused by coating layer LNO. The DFT calculation shows that LNO, the main phase of the coating layer, is a high-hardness material (the mechanical parameters are shown in Tables S9–S11, Supporting Information). The shear modulus of LNO is 124.17 GPa, which is remarkably more considerable than that of NCM88. Therefore, the

coating layer LNO has the greater influence on , shown in Figure 2b. Additionally, the curvature of the $E_{\text{Coating-x}}$ curve (0.46 V/atom) is more serious than that of $E_{\text{Formation-x}}$ (0.35 V/atom) during the H1 and H2 phase transitions. Therefore, the pure phase of $\text{Li}_{1-x}[\text{Ni}_{0.84}\text{Co}_{0.08}\text{Mn}_{0.08}]\text{O}_2$ tends to be formed rather than the binary phase, corresponding to a split of the (003) plane at 20–30 ks in XRD (Figure 2i). For H2 and H3 phase transitions, the E_{Coating} of the H3 phase is increased with the LNO coating. The difference of formation energy between the H3 phase and H2 phase of NCM@LNO is decreased to 0.064 eV, compared with that in the pristine system (0.15 eV). When the formation energy gap between the H3 and H2 phases is small enough, the pure H2 phase can be easily kept without phase transition. In addition, the pure phase of the NCM material is also funded by the high curvature of H1 and H2 during delithiation. As a result, the types of internal phases tend to be homogeneous, and the formation of the most harmful H3 phase could be delayed through the coating so as to improve the cycle and mechanical stability.

It is demonstrated that the LNO coating theoretically suppresses the generation of the miscible phase and delays the phase transition. If the phase transition of a secondary particle is suppressed with the evenness of the phase, the distribution of lithium ions in the bulk must be uniform (this will be explained in the following content). As a result, the evenness of the phase in the particle will be further promoted, thus making the mechanical structure of the particle more stable.

2.2. Structure of the Constructed Materials

The ultra-high nickel ternary cathode $\text{LiNi}_{0.88}\text{Co}_{0.10}\text{Mn}_{0.02}\text{O}_2$ (NCM88) is prepared through the conventional co-precipitation method. (9,30) Inductively coupled plasma mass spectrometry is used to determine the atomic composition of the material with the normalized formula NCM88 as the pristine sample is analyzed (Table S1, Supporting Information). LiNbO_3 (LNO) coating with a stable structure was obtained as guided by the phase diagram (Figure 1h, Supporting Information). According to the mass fraction of the coating layer, the as-obtained materials are named pristine, 1% LNO, 3% LNO, and 5% LNO (corresponding to 0, 1, 3, and 5% of the total mass of the coating layer in the cathode material). Characterized by XRD, the structure and composition of the coating layer on the surface of the measurement sample are effectively confirmed, and the percentages of different components are also roughly gained. (31)Figure 3b shows that the characteristic peaks of the obtained samples are similar, and all the peaks could be indexed to the $\alpha\text{-NaFeO}_2$ -type hexagonal structure of the space group $R\bar{3}m$. Besides, a bimodal feature of the (006)/(012) and (018)/(110) peaks at $\approx 38^\circ$ and 65° , respectively, is prominent, which provides signs of a classic layered structure, (32) indicating that the explored coating method maintains the original structure of the material. (33) Significantly, the intensities of (003) and (104) diffraction peaks for the pristine sample are stronger than those of the

other modified samples, implying that the basic material is protected by the coating layer, suggesting that the coating layer is uniformly adhered on the surface of NCM88 (Figure 3b). (31) As shown in Figure 3c, the peak positions of the (003) and (104) peaks are slightly shifted to lower angles, indicating that both the lattice parameters c and a are increased simultaneously. In addition, according to the value of the lattice parameter obtained by Rietveld refinement of XRD (Figures 3d,e, S2, and Table S2, Supporting Information), it is confirmed that a part of the Nb element is effectively doped into the bulk phase. For the modification sample, the coating layer is composed of LiNbO_3 (LNO, space group: $R3c$) and Li_3NbO_4 (space group: $I23$). Through Rietveld refinement of XRD, it is found that the LNO-coated NCM811 has been successfully prepared. However, no character diffraction peaks of LNO are noticed in the XRD curves for pristine and 1% samples, which could be attributed to its low contents. However, they are observed (marked the position of ▼, approximately between 42° and 43°) when the proportion is increased up to 3 wt % (Figure 3b). Moreover, in Figure 3a, it is also evidence of successful preparation of the LNO layer surrounding the Ni-rich cathode that the diffraction peak of 10% LNO is noticed. Furthermore, as listed in Table S2 (Supporting Information), the $I(003)/I(103)$ value of modified samples is declined with the doped Nb (Figure 3b,c), which suggests the increase of cation mixing degree. When Nb^{5+} is doped, Ni^{3+} is reduced to Ni^{2+} to maintain charge neutrality. Moreover, Ni^{2+} (0.69 \AA) would replace Li^{+} (0.76 \AA) sites due to the similarity of their radius, resulting in the slightly increased cation mixing, which can make the lattice structure more stable to some extent. (34–36)

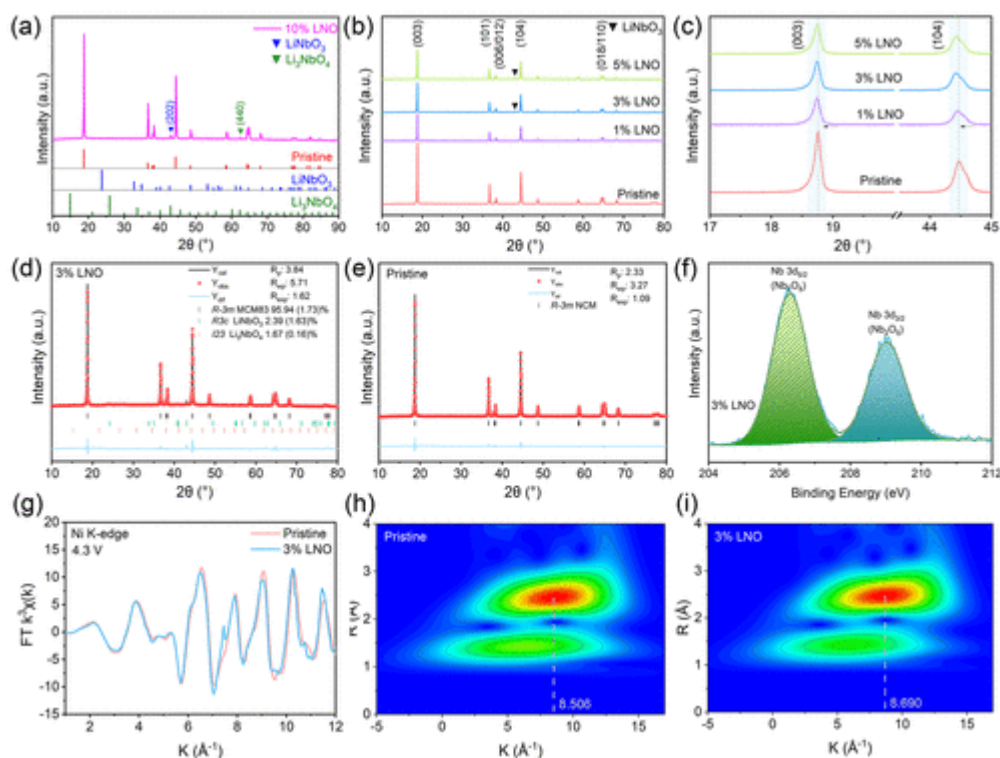


Figure 3. Structure analysis of the samples. (a) XRD pattern of the 10% LNO sample. (b) XRD patterns of the as-obtained samples. (c) Enlarged image of the (003) and (104) diffraction peaks. Rietveld refinement result of 3% LNO (d) and pristine (e) samples. (f) High-resolution XPS spectra of Nb 3d for 3% LNO. (g) EXAFS fitting curves at the k space of pristine and 3% LNO. WT for the k^3 -weighted EXAFS signals of (h) pristine and (i) 3% LNO.

The morphology and composition induced by the coating are characterized by scanning electron microscopy (SEM). As shown in Figure S3 (Supporting Information), both the original and processed samples are composed of spherical secondary particles with a size between 5 and 20 μm , most of which are larger than 10 μm in diameter. Large enough particles densely stacked by primary nanoparticles (~ 250 nm) are necessary to ensure that the coating phase remains intact on the surface of the material. (37,38) As the content of LNO is increased, it is clear that the surface of the secondary particles becomes denser and smoother, and the textures on the surface are gradually filled with the coating. Energy-dispersive X-ray spectroscopy (EDX) elemental mapping was utilized to reveal the element distribution. As shown in Figures S5–S8 (Supporting Information), the distribution of Ni, Co, Mn, and O is quite uniform as expected. The Nb element does not exist in the pristine sample, and as

the content of LNO is improved, the distribution of the Nb element around the original sample becomes more and more obvious, indicating that LNO is uniformly coated on the surface of NCM811.

Focused ion beam (FIB) is employed to cut the secondary particles with 3% LNO coating, aiming to explore the coating layer. It is confirmed that Nb is much enriched in the coating, and Ni, Co, Mn, and O are included in the bulk (Figure 4k). In addition, a small amount of the Nb element is also observed in the bulk phase, agreeing well with the results of XRD Rietveld. Furthermore, to investigate the microstructure and chemistry of the modified sample, high-angle annular dark field-scanning transmission electron microscopy (HAADF-STEM) is utilized, and the image is shown in Figure 4. HAADF-STEM images along the [001] zone axis and the corresponding fast Fourier transform patterns confirm the presence of $R\bar{3}m$ NCM and $R3c$ LNO. At the same time, a transition region at the junction of two phases is also noticed (see in Figure 4g). The inner layer corresponds to the plane (006) and the plane (110) at an angle of 90° , shown in Figure 2h. Moreover, a coating layer with a thickness of approximately 12 nm is found seen as the outer layer, (110) and (300) are marked, and the angle between them is 45° (Figure 2i), further indicating that the LNO coating layer has been uniformly distributed on the surface of NCM88.

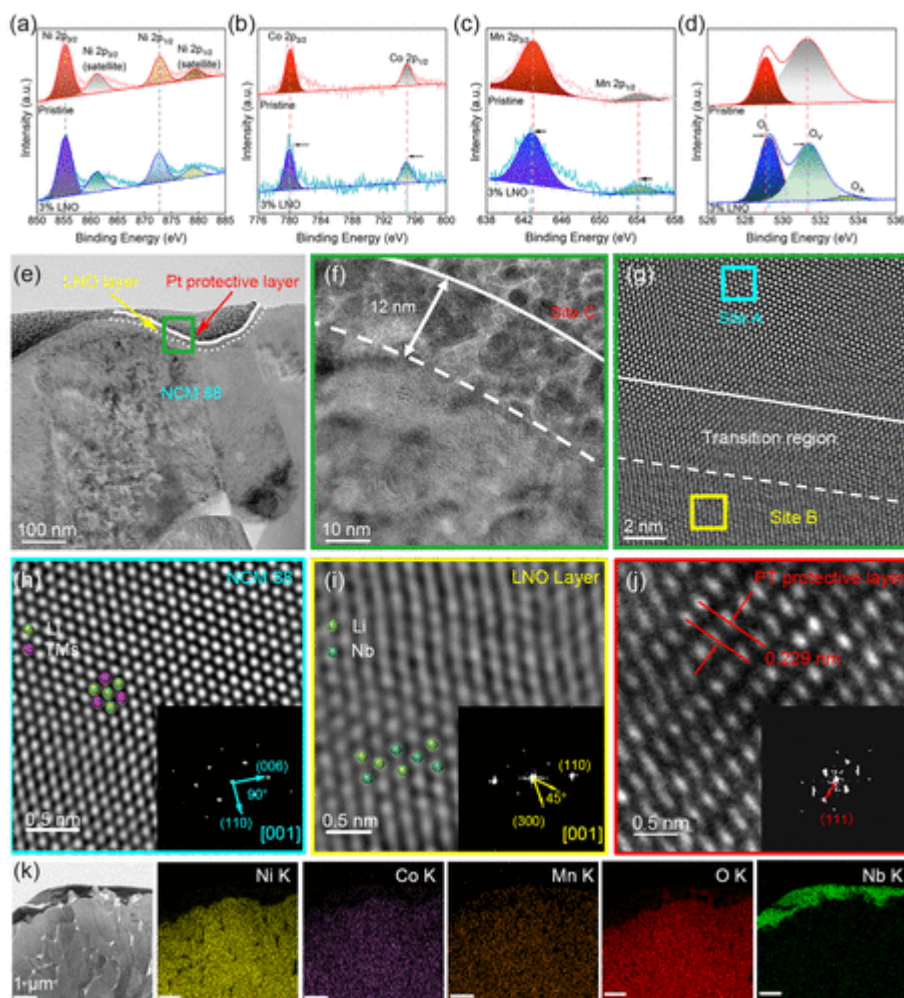


Figure 4. High-resolution XPS spectra of (a) Ni 2p, (b) Co 2p, (c) Mn 2p, and (d) O 1s pristine and 3% LNO samples. (e,f) HRTEM of 3% LNO, (g) HAADF-STEM image of the junction of the 3% LNO sample bulk and coating layer, (h–j) HAADF-STEM image of the bulk phase, LNO coating, and Pt protective layer. (k) EDS results show the element distribution of the secondary particles.

XPS analysis also provides clear evidence for the successful LNO surface modification on NCM88. XPS spectra of Ni/Co/Mn 2p and O 1s of pristine and 3% LNO samples are presented. Figure 3f demonstrates one of the XPS spectra of the 3% LNO sample, in which the Nb signal can be clearly detected in the LNO-decorated samples, which was absent in the pure NCM88 material. Specifically, the binding energies of Nb 3d orbitals are located at ≈ 206.33 and 209.33 eV, consistent with the Nb⁵⁺ ion in LiNbO₃ (LNO) and Li₃NbO₄, respectively. It is worth noting that the main fitting peaks of Ni 2p are not shifted at all (Figure 4a). In contrast, the peaks of Co/Mn 2p of 3% LNO have a slight offset

toward a lower binding energy (Figure 4b,c), showing that Nb⁵⁺ may influence Mn or Co sites. (39) This phenomenon above is in good line with the Rietveld refinement of XRD. As shown in Figure 4d, all the O 1s spectra can be deconvoluted into three fitting peaks, corresponding to the lattice oxygen (OL), oxygen vacancy (OV), and adsorbed oxygen (OA) at around 529/531/533 eV, respectively. Interestingly, the intensity of binding energy of OL is increased with the coating layer (Figure S4a, Supporting Information), confirming that Nb⁵⁺ has a strong coupling effect at the interface, leading to the increase of strong metal–oxygen bonds and thereby improving the stability of the material and promoting charge transfer. In addition, the fact that the O 1s peak is generally moved to a high-energy direction also indicates that the introduction of strengthened oxygen bonding in the surface region of the particle is mainly derived from the Nb–O bonds in the outer LNO layer. The EXAFS fitting curves of at the k space of pristine and 3% LNO samples are shown in Figure 3g, so the wavelet transforms (WTs) for the k³-weighted EXAFS signals are obtained, which can also further confirm the doping of Nb⁵⁺. As shown in Figure 3h,i, the peak of 3% LNO is shifted to a high-angle direction, showing the introduction of heavy atoms. (40)

2.3. Enhancement of Mechanical Performances

To further verify the calculated results in this work about how the LNO coating alleviates the deleterious phase transition, in situ XRD experiments are carried out for the first cycle in the range of 2.5–4.3 V at 40 mA g^{−1}. Figure 2f,i shows the contour plots of selected regions of the in situ XRD patterns, accompanied by the corresponding voltage curves of the cells concerning the charging time. Indeed, as shown by in situ XRD during electrochemical cycling, the same bulk phase transition and lattice expansion/shrinkage were observed in pristine and 3% LNO samples. In addition, the cathode suffers from a series of phase transitions, which are well consistent with that revealed by the dQ dV^{−1} curves (Figure 1e). (15,41) Furthermore, the peak intensity representing the H2 → H3 phase transition is reduced, indicating that the phase transition intensity is decreased. (42,43) The (003) reflections, depicting the unit cell dimension in the c-direction, are plotted as a function of the charge voltage in Figure 2f,i. The split at about 3.9 V represents a mixture of H1 and H2 phases (Figure 2f), which conforms to the calculation result above (Figure 2a). On the contrary, the (003) reflections for the modified sample exhibit a smooth transition from the H2 → H3 phase, whereas a rather abrupt shift of the (003) reflection is observed at 4.2 V for the pristine sample. In conclusion, the phase transition is delayed and effectively suppressed, leading to less mixed phases. (44–47)

Moreover, as shown in Figure S12g,h (Supporting Information), cyclic voltammetry (CV) tests with varied scan rates were carried out to explore the changes for the phase transition, and distinct changes are observed on the curves. The peak for the H2 → H3 phase transition is moved gradually to a higher

potential. In addition, a linear relationship of potential (V) versus scan rate (mV/s) is presented, and the slope is regarded to assess the relative rate of phase transformation, as displayed in Figure S12i (Supporting Information). (37) The transformation rate (the slope) of the 3% LNO sample is about 3.961, much smaller than that of the pristine sample (4.474), demonstrating its optimized structure stability, which shows that the beneficial cycle stability of the 3% LNO sample is realized by a slight structural fluctuation during its cycle, agreeing with the calculated result.

As proposed in Section 2.1, the cause of phase variation is the inherent instability of the $\text{Ni}^{3+}/4+-\text{O}2-$ structure. (48) During the delithium process, $\text{Ni}^{2+}/\text{Ni}^{3+}$ is gradually oxidized to Ni^{4+} with a smaller ion radius resulting from the charge compensation mechanism. (49) Therefore, when the regions of excessive delithiation (H3 phase) occur in the Ni-rich cathode, the amount of Ni^{4+} in the secondary particles is increased. Accordingly, when the secondary particles have the same degree of delithium (the total amount of lithium-ion removal is the same), the even distribution of lithium ions determines the content of active Ni^{4+} in the system. Considering Ni^{4+} is harmful to the stability of the structure during charging and discharging, it can bring a shrinking hTM–O and irreversible side reactions with the electrolyte. Therefore, the evenness of lithium-ion distribution in secondary particles plays an important role in the stability of the Ni-rich cathode structure. Hence, the content of Ni^{4+} is utilized to prove the uniformity of lithium-ion distribution during charging and discharging. The average oxidation state of Ni ions can be attained by comparing the measured spectral features with that of a linear combination of Ni^{2+} , Ni^{3+} , and Ni^{4+} . In the case of the Ni L-edge shown in Figures 5a and S13a,b (Supporting Information), the peaks at 853 and 855 eV illustrate a good match with the character peaks of Ni^{2+} (~ 852.8 eV) and Ni^{4+} (~ 855 eV). (50,51) By comparing the valence states of Ni ions in the materials under the original and after 10 h of a 4.3 V constant voltage charging state, it is found that the proportion of Ni^{4+} in the materials after charging is significantly enlarged. For pristine NCM under the 4.3 V charged state, the $\text{Ni}^{2+}/\text{Ni}^{4+}$ ion intensity is 0.972:1.243. However, for the 3% LNO sample, it is 0.972:0.991 (Figure 5a), revealing that LNO coating plays a significant role in mitigating the excessive valence of Ni ions, which also means that the uniformity of lithium-ion distribution is improved during the charging process after coating. This result is consistent with the DFT calculation outcomes (Figure 2a–c). In addition, the evidence about the O 2p-TM 3d hybridized feature could verify the electron transfers from Ni to O in the bulk, as shown in Figure 5d, and it occurs in the photon energy range of 527–534 eV. Besides, the O 2p-TM 3d hybridization feature at ~ 529 eV for the 3% LNO sample is much less severe than that of the pristine sample. Moreover, Figure 5b,c shows that for the pristine and 3% LNO samples, no difference is observed in the peaks of Mn and Co. All the proofs above indicate that the valence state change of Ni during charging is the most crucial reason for the difference in the properties of the two samples. Hence, Ni^{4+} and the evolution of O in the bulk are

generated by the hybridization of Ni ions and O ions. The significant difference between the pristine and 3% LNO samples about the peak intensities at 529 eV reflects that the LNO layer is helpful to reduce the harmful hybridization in the Ni-rich cathode.

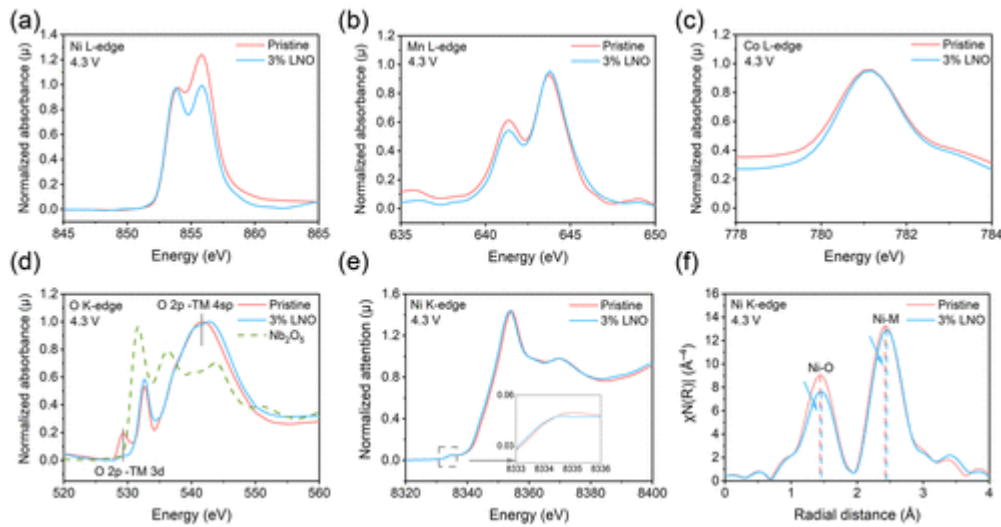


Figure 5. Soft XAS spectra of (a) Ni L-edge, (b) Mn L-edge, (c) Co-edge, and (d) O K-edge for pristine and 3% LNO charge to 4.3 V. (e) EXAFS of the pristine and 3% LNO samples. (f) Ni K-edge XANES spectra and an enlarged view of the pre-edge.

To investigate the charge compensation on lithium-ion extraction over the first cycle in the NCM cathode, the Ni K-edge XANES experiment is performed. It shows that the shift toward a higher energy in the Ni K-edge is noticed during charging, which is well consistent with the expectation that Ni³⁺ is oxidized to Ni⁴⁺. (49) To demonstrate that the LNO coating can indeed reduce the production of Ni⁴⁺ with even delithiation, Ni K-edge values of pristine and 3% LNO samples are compared at the 4.3 V charged state (see in Figure 5e). Obviously, the curves of the modified sample have a shift to a lower-energy region compared with the pristine sample after charging, showing that the generation of Ni⁴⁺ in the bulk phase is indeed well suppressed, clearly revealing that the phase transformation of the modified sample is reduced. Moreover, the pre-edge is generally considered as a better oxidation state measure than the main edge. (52) The intensity of the pre-edge of the two samples is slightly different, with the modified sample lower than the pristine (insets of Figure 5e). The peaks arise from the quadrupole-allowed transition from the Ni 1s state to the Ni 3d state, which typically arise in distorted octahedral TM sites. (53) The increase of peak intensity symbolizes a slight distortion of centro-symmetry caused by the mixing between the Ni 3d and 4p states. Furthermore, the phenomenon that the shift for the pre-edge of the pristine sample in the direction of a high energy indicates that Ni is oxidized. In general, XANES spectroscopy clearly proves that LNO coating has a

strong inhibitory effect on the excessive and malignant oxidation of Ni, which is in line with the DFT calculation results (Figure 2b).

Moreover, pair distribution function (PDF) analysis is employed to verify the detection of short-range disorders. (54) As proved in Figure 5f, the positive displacement of the first peak of PDF in the 3% LNO sample implies that the shrink of Ni–O bonds during charging is not as severe as that of the pristine sample. (55) Meanwhile, the distance between Ni atoms of the modified sample is longer than that of the pristine sample, suggesting that the phase transition of the modified material which causes the cell parameter shrinkage is well alleviated at a 4.3 V cutoff voltage, which is in good agreement with the results of the in situ XRD analysis. This difference also induces an easier delithiation configuration (i.e., reduces the energy barrier for lithium-ion diffusion) since the modified sample exhibits a lower Ni–O bond energy during charging (a longer Ni–O bond) than the pristine. Thus, the binding of the Li–O bond will be weakened considering that the O atoms are also bonded with Li atoms, leading to the faster diffusion of lithium ions. Therefore, the diffusion barrier of the modified cathode is reduced (will be further proved below), thereby evening the distribution of lithium ions in the bulk phase and ultimately suppressing the H2 → H3 phase transition.

2.4. Improvement of Electrochemical Performances

The coin-type half cells are fabricated by utilizing the samples as electrode materials to evaluate the storage performances within a voltage range of 2.5–4.3 V. The modified samples display superior cycle stability and rate performances, in which the 3% LNO electrode shows the best electrochemical performances among the samples. As shown in Figure 6a,b, the capacity retentions of the NCM88, 1, 3, and 5 wt % LNO samples are 36.09% (65.5 mA h g⁻¹), 56.12% (116.9 mA h g⁻¹), 74.96% (127.4 mA h g⁻¹), and 50.91% (83.8 mA h g⁻¹) after 300 cycles at 2 C and 43.37% (71.7 mA h g⁻¹), 54.36% (89.2 mA h g⁻¹), 62.83% (98.9 mA h g⁻¹), and 51.14% (80.8 mA h g⁻¹) after 500 cycles at 5 C, respectively. In addition, Figure S12c,f (Supporting Information) shows the CV results of NMC88 cycled at voltages between 2.5 and 4.3 V with a rate of 2 C, and the 3% LNO sample renders slower performance decay, with a capacity retention of 74.94%, demonstrating that the capacity decay of the positive electrode material is effectively suppressed. The worsening of the pristine Ni-rich cathode performance can be partially ascribed to the thickening of the disorder rock salt layers and the irreversible structural changing (such as the microcracks caused by a phase transition).

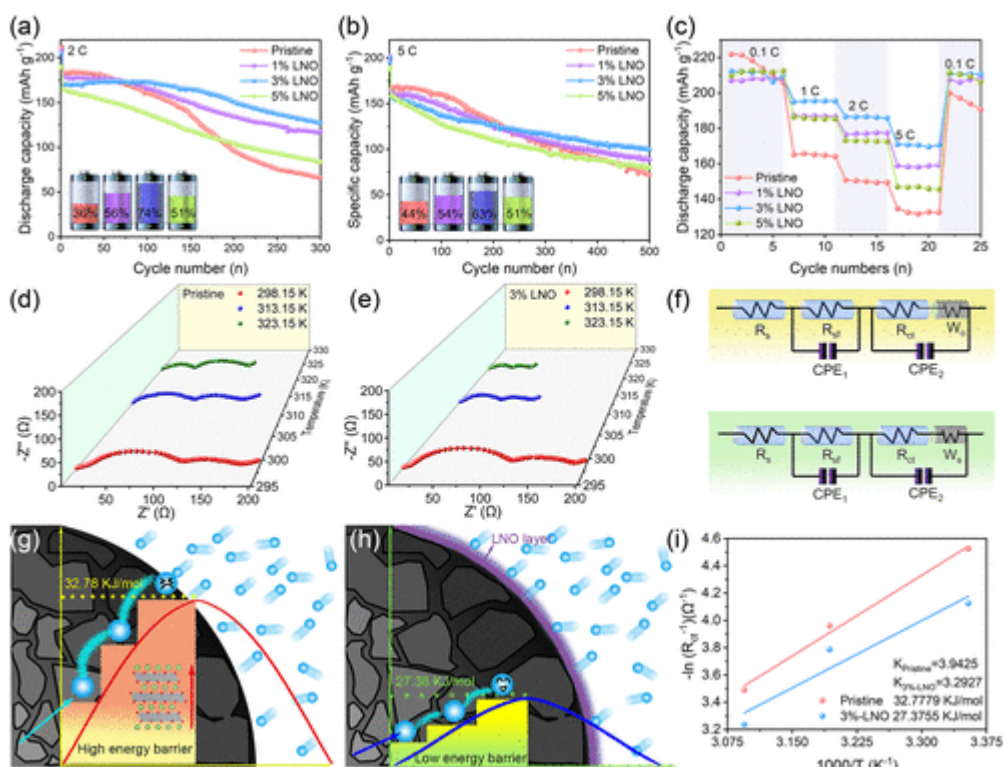


Figure 6. Cycle performance of the as-obtained samples at 2 (a) and 5 C (b). (c) Rate performance of the as-obtained samples. Charge-transfer mechanism of the as-obtained samples. EIS spectra of different temperatures (d,e). The equivalent circuit before the cycle is yellow on the top (f), and the green one after the cycle on the contrary (f). The LNO layer significantly reduces the energy barrier for lithium-ion transmission (g,h). Arrhenius plot for the Rct and activation energy of the charging process of pristine and 3% LNO samples (i).

Moreover, the 3% LNO sample again exhibits the best capability under different rates (Figure 6c), which delivers a larger capacity of 170.7 mA h g⁻¹ at a high rate of 5 C over that of the pure NCM88 (131.7 mA h g⁻¹). Since the transport rate of lithium ions is the main factor restricting the rate performance, it is speculated that the LNO layer may promote the transport rate of lithium ions due to the excellent ionic conductivity (10–5 cm² s⁻¹) at room temperature. (56)

In addition, pristine NCM88 and 3% LNO show dramatically different microstructures after cycling. After 500 cycles under a 5 C discharge rate at 25 °C, severe damaged and corroded secondary particles of the pristine sample are observed with SEM (Figure 7). On the contrary, the 3% LNO sample has an excellent mechanical structure with a smooth surface. By analyzing the morphology of the material after cycling, it is concluded that the outstanding performance of the modified sample is achieved by

the combined effect of the improvement of the interface stability and the progress of the mechanical properties in the bulk phase.

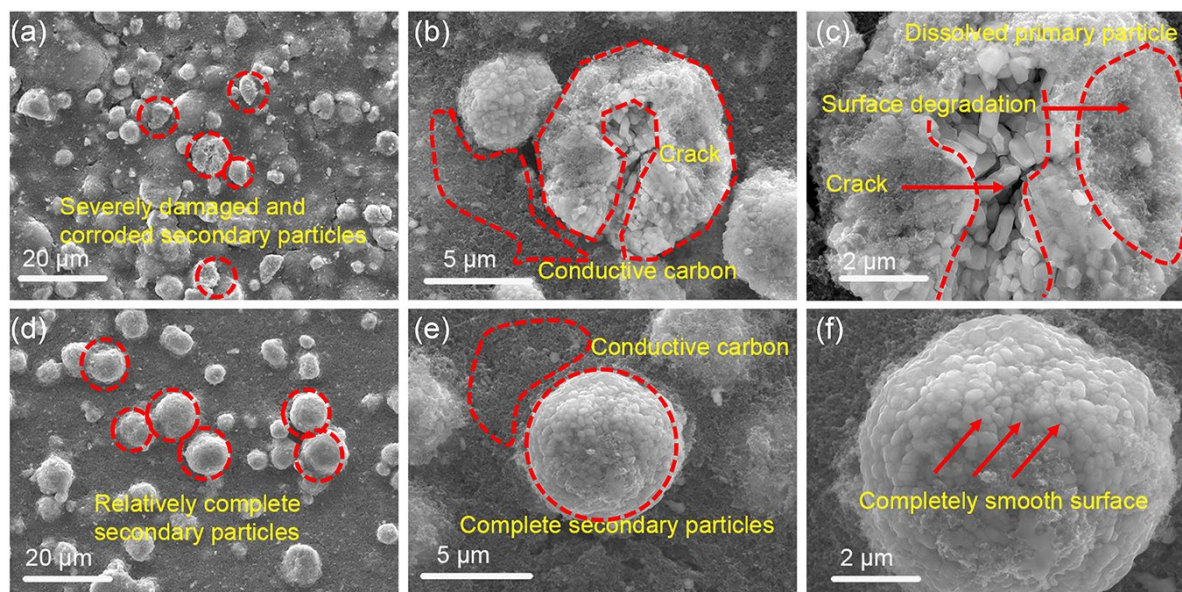


Figure 7. Morphology of the pristine sample (a–c) and 3% LNO sample (d–f) after 500 cycles at 5C.

The improvement of the electrochemical properties by the LNO layer can be divided into three aspects. It can protect the cathode from having side reactions with the electrolyte to improve the cycle stability. The lithium-ion distribution kinetics at the interface is improved; thus, there is advancement of rate performance. (57) Finally, the evenness of lithium-ion distribution at the surface of the particles is increased, thereby promoting the uniformity of the internal phase of the particles. (14) Therefore, the improvement of the overall performance can be summarized as the “chemistry-mechanics effect”, indicating that this kind of chemical development can also play a role in promoting mechanical stability; that is, the internal phase is evened by the homogeneous distribution of lithium ions, which can be beneficial to the maintenance of the structure.

By analyzing the composition of the cathode surface after cycling, the level of surface side reactions can be intuitively assessed. The interface of cycled samples was characterized by XPS, in which the signals of C 1s are provided by organic CEI components, such as polycarbonates and semicarbonates. (58–60) The existence of C–C and C–H bonds is ascribed to the binder and conductive substance in the electrodes, whereas C=O and C–F/OCO₂ bonds are assigned to the decomposition of carbonate electrolyte solvents. The peak area of C=O for 3% LNO-NCM is close to 0 (Figure 8h), suggesting that the corrosion of the electrolyte is inhibited. Ni 2P signals are contributed by CEI components, such as

NiF₂. A smaller peak area of Ni 2P_{3/2} and Ni 2P_{1/2} for the 3% LNO sample is observed, demonstrating the formation of less irreversible side reactions over the pristine sample (Figures 8i and S4b, Supporting Information). (10) At the same time, the peak corresponding to the P–F moiety in CEI is lower in modified samples (Figure 8g), indicating that the LNO layer suppresses the decomposition of LiPF₆. (61)

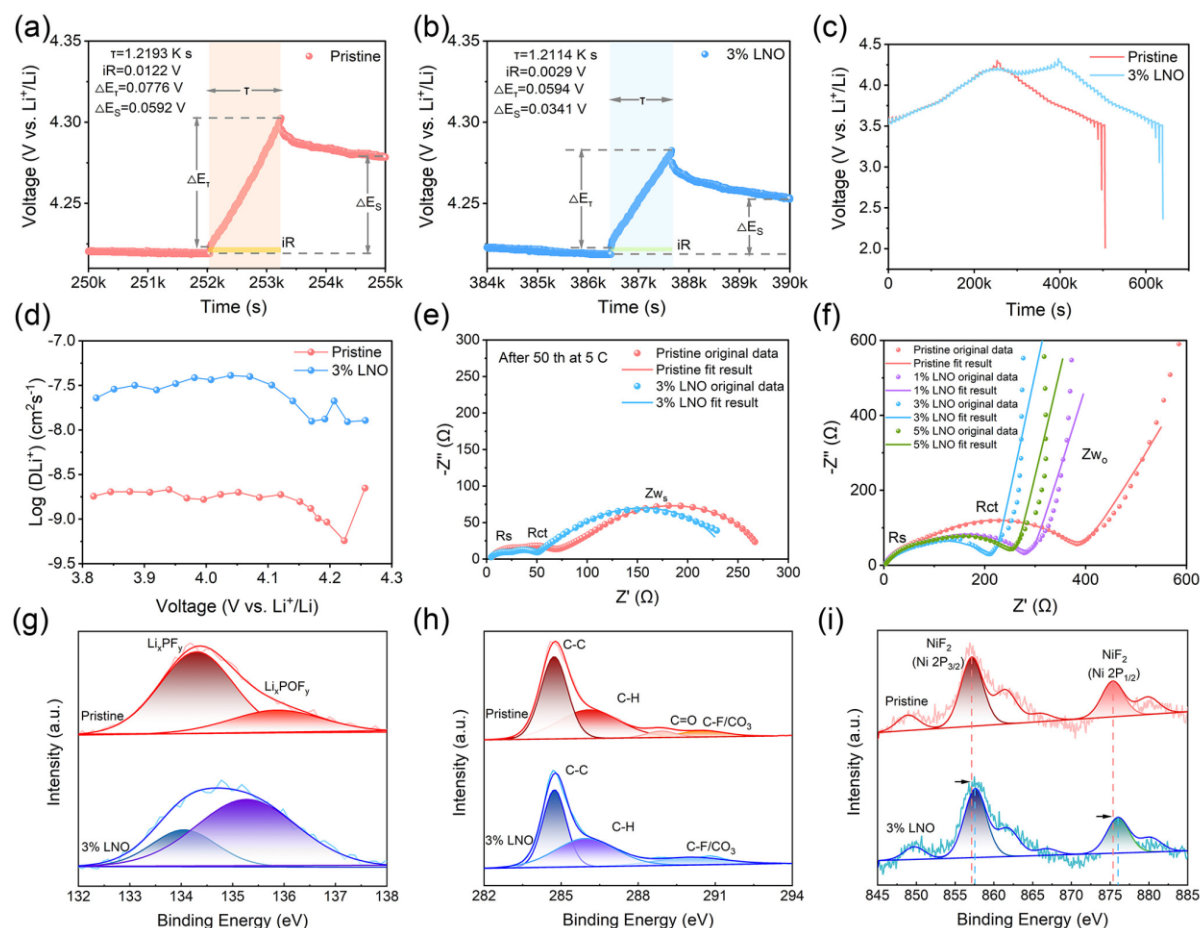


Figure 8. GITT characterization of samples. Transient charge voltage at 4.2–4.3 V of the pristine sample (a) and 3% LNO (b). (c) Transient charge voltage profile. (d) Comparison of lithium-ion diffusion coefficient between pristine and 3% LNO. (e) Impedance comparison after 50 cycles at 5C. (f) Impedance comparison before cycling. XPS spectra and composition analysis of (g) P 1s, (h) C 1s, and (i) Ni 1s for the electrodes after 500 cycles.

Moreover, EIS was performed to explore the enhanced rate performance of the samples. According to the simplified interface models presented with the corresponding equivalent (Figure 6f), the electrochemical resistance between the electrode and electrolyte can be determined. (62,63) R_s is regarded as the series resistance, such as the bulk resistance and resistances from the separator and

electrodes. (59,64) R_{ct} represents the charge-transfer impedance revealed in the high-frequency region. (60,65) R_{sf} means the conductive impedance of Li^+ through the CEI in the medium-high frequency region. (66) The low-frequency region is associated with Warburg impedance (W_o), and the Nyquist plot presents as a declining line in the area, corresponding to semi-infinite diffusion. (67–69) Before the cycle, the plots in the high-frequency range display the semicircle profiles (Figure 8f), which are attributed to a surface charge transfer process. (70) As calculated from the EIS data, the R_{ct} of 3% LNO is about 155.9 Ω , which is lower than that of the pristine (329.5 Ω), 1% LNO (200.5 Ω), and 5% LNO (169.9 Ω) (see Table S3, Supporting Information and Figure 8f), which have similar characteristics with the R_{sf} . This shows that the coating layer can bring a high electronic conductivity and ion conductivity, thus promoting the even distribution of lithium ions and electrons. (71) In addition, as shown in Figure 8e, after 50 cycles at 5 C, the Nyquist plot of the samples looks like an arc in the low-frequency region, corresponding to a finite Nernst diffusion process. (69,72) Obviously, after cycling, the R_{sf} and R_{ct} of the pristine are lower than those of 3% LNO, indicating that LNO inhibits the occurrence of surface side reactions, which is well consistent with the results of XPS analysis (Figure 8g–i).

Activation energy at different temperatures can symbolize characters of the ionic conductivity, as shown in Figure 6d,e. A typical Arrhenius equation is used to evaluate the degree of difficulty of lithium-ion transport

$$\frac{1}{R_{ct}} = A_0 \exp\left(\frac{-E_a}{RT}\right) \quad (2.3)$$

where A_0 is an exponential factor that is a constant for a given chemical reaction, related to the frequency of particle collision; E_a is the activation energy of the reaction (usually given in Joules per mole or J/mol); R is the universal gas constant; and T is the absolute temperature (in Kelvins). (73,74) After being cycled at 0.1 C and then charged at a 3.7 V constant voltage for 10 h, the coin-type half battery was used to measure the R_{ct} at different temperatures. It is found that under the induction of LNO coating, the corresponding energy barrier for the charge transfer in the modified samples is alleviated (Figure 6g,h). The corresponding E_a for the pristine and 3% LNO electrodes are about 32.7779 and 27.3755 kJ mol^{-1} (as shown in Figure 6i), respectively. The 3% LNO sample displays a 16.48% reduction of the energy barrier for the charge-transfer process in contrast to the pristine sample, which is well consistent with the PDF analysis in Section 2.3.

To further understand the mechanism of ionic conductivity improvement, GITT was employed to investigate the lithium-ion diffusion kinetics of pristine and 3% LNO samples. As shown in Figure 8a,b, the electrochemical polarization can be evaluated by analyzing a selected point on the charging platform (approximately 4.2 V). The ΔE_t and ΔE_s of the pristine sample are higher than the

corresponding values of 3% LNO, showing the reduced polarization in the 3% LNO sample. Also, the side reaction during the charging process for 3% LNO is efficiently suppressed, which is consistent with the result of XPS and EIS. (75) Furthermore, as shown in Figure 8d, the lithium-ion diffusion coefficients of the 3% LNO sample are overall larger than that of the pristine sample after one cycle under 0.1 C (the overall GITT voltage response curves are shown in Figure 8c). Moreover, the H2 → H3 phase transition in the $dQ/dV-1$ curve corresponds to a sharp decline in the plot of the calculated lithium diffusivity (Figure 1e). (41) The lithium-ion diffusion coefficient for the pristine sample decreases abruptly during the H2 → H3 phase transition (4.2 V), but that for the 3% LNO cathode decreases gently, reflecting a slight phase transition (Figure 8d). Therefore, the generation of the H3 phase can affect the lithium-ion diffusion coefficient, which means that the internal structure influences the performance at the surface.

3. Conclusions

To summarize, an LNO-coated coupled Nb⁵⁺-doped NCM88 cathode with crack-free instruction is successfully obtained. Mechanically, according to the result of DFT calculations, the tendency of phase transition (H1 → H2 → H3) is significantly alleviated by the excogitated of the interface force invoked by the LiNbO₃-functionalized coating layer. Meanwhile, the rigidity of the crystal structure is remarkably strengthened by constructing the Nb–O binding activated with Nb⁵⁺ doping. Chemically, the robust electrode/electrolyte is driven from the functionalized shielding layer, which is conducive to protecting the electrode against electrolyte corrosion along with subsequent transition metal dissolution, ultimately rendering a faster/highly convertible lithium-ion diffusion. As a result, an ultrahigh cyclic and structural stability can be achieved by improving the mechanical and chemical aspects at the same time. More encouragingly, this mechanics/chemistry strategy can contribute to the development of a crack-free Ni-rich cathode to meet the needs of consumers for a new generation of lithium-ion batteries.

4. Experimental Section

4.1. Chemicals

All chemicals were purchased from Aladdin, without any supererogatory purification. They were used to synthesize the target samples.

4.2. Materials Synthesis

The synthesized $\text{LiNi}_{0.88}\text{Co}_{0.10}\text{Mn}_{0.02}\text{O}_2$ (NCM88) material is heated and stirred in a water bath at 80 °C according to a certain stoichiometric ratio with a mixed solution of ammonium niobate oxalate and lithium hydroxide ($\text{LiOH}\cdot\text{H}_2\text{O}$). (56) Heating and stirring are continued until the suspension evaporates to dryness; then, the powder is scraped out and turned into a solid. After the powder is sufficiently ground, it is transferred to a tube furnace. First, the temperature is increased to 400 °C at a heating rate of 1.5 °C/min and then calcined for 5 h. Then, the temperature is increased to 750 °C at a heating rate of 1 °C/min, and the calcination is performed for 10 h. The results show that according to the LiNbO_3 content of different mass fractions, the obtained materials are named 1% LNO, 3% LNO, and 5% LNO.

4.3. Materials Characterizations

The crystalline structure of composites was determined using a Rigaku Ultima IV powder X-ray diffractometer with a $\text{Cu K}\alpha$ radiation ($\lambda = 1.54059 \text{ \AA}$, 40 kV, 50.0 mA), scanned over a range of 5–120° at a scan rate of 0.05°/step. The morphology, elemental distribution, and microstructure of composites were measured by high-resolution field emission scanning electron microscopy (TESCAN MIRA3 LMU) equipped with an EDS energy-dispersive X-ray spectrometer. STEM specimens were prepared by FIB lift out using an FEI Helios NanoLab G3 UC FIB operating at 2–30 kV. The as-prepared STEM specimens were investigated using an FEI Titan Cubed G2 60–300 aberration-corrected TEM/STEM at 300 kV. Sub-angstrom resolution images were obtained using the STEM-HAADF detectors with the inner and outer collection angles at 79.5 and 200 mrad, respectively. The HAADF images presented here were Fourier-filtered to minimize contrast noise. The XPS (PHI 5000 VersaProbe III) measurements were performed to perceive the valence state of relative elements and investigate the changes of the surface composition for as-prepared composites and electrodes with monochromatic $\text{Al K}\alpha$ (1486.6 eV) radiation operated at 72 W (6 mA, 12 kV) in a vacuum of about 2×10^{-7} mba. The Ni/Co/Mn L-edge and O K-edge were measured at the beamline U19 of the National

Synchrotron Radiation Laboratory (NSRL, Hefei) in the total electron yield mode by collecting the sample drain current under a vacuum better than 10^{-7} Pa. The Ni/Co/Mn/Se K-edges were collected at the BL11B station in the Shanghai Synchrotron Radiation Facility (SSRF, operated at 3.5 GeV with a maximum current of 250 mA). STEM specimens were prepared by FIB lift out using an FEI Helios Nanolab G3 UC FIB operating at 2–30 kV. First, a 1.5 μm thick Pt layer (200 nm electron beam deposition, followed by 1.3 μm ion beam deposition) was deposited on the region to be extracted to avoid damage by the Ga ion beam and to protect the coating. Then, the specimens were thinned to ~ 200 nm using a 30 kV Ga ion beam; a 5 kV Ga ion beam was used to thin to ~ 150 nm. Finally, 2 kV Ga ions were utilized for final polishing to remove the surface damage layer and for further thinning to electronic transparency. The as-prepared STEM specimens were investigated using an FEI Titan Cubed G2 60–300 aberration-corrected TEM/STEM at 300 kV. Sub-angstrom resolution images were obtained using the STEM-HAADF detectors with the inner and outer collection angles at 79.5 and 200 mrad, respectively. The HAADF images presented here were Fourier-filtered to minimize contrast noise. EDS analysis was carried out using a Bruker Super EDX detector and a Gatan Image Filter Quantum-966 system.

4.4. Electrochemical Measurements

Using NMP as a dispersant, the active material, super phosphorous and polyvinylidene fluoride were mixed at a mass ratio of 7:2:1 to prepare a working electrode. (76) The slurry was then spread on Al foil and dried at 120 °C in a vacuum oven. The mass loading of each electrode is about 3 mg cm^{-2} . The CR2016 coin-type lithium half-cells were assembled in a glovebox filled with argon gas using the Celgard 2400 membrane as the separator and 1 M LiPF₆ in EC/DEC (1:1) as the electrolyte. The cycling and rate performances were tested on a Neware battery testing system (Neware Co., Ltd, Shenzhen) at varied current densities. CV and EIS were investigated by using the Autolab (MULTI AUTOLAB M204) electrochemical workstation.

4.5. DFT Calculations

The first-principles calculations were performed within the DFT (77,78) framework by using the Vienna ab initio simulation package (79) and the projector augmented-wave method (80) with the Perdew–Burke–Ernzerhof generalized gradient approximation. (81) According to the former reports, (82) the Hubbard U correction parameters (83) ($U_{\text{eff}} = U - J$) of Ni, Co, and Mn were set to be 6.2, 3.32, and 3.9 eV, respectively. The plane-wave cutoff energy was 500 eV. The total energy and residue atomic force were converged up to 10^{-4} eV and 0.05 eV \AA^{-1} , respectively. (83) $2 \times 2 \times 1$ supercells of $\text{Li}_{1-x}\text{Ni}_{0.84}\text{Mn}_{0.08}\text{Co}_{0.08}$ were used for the calculation. The Brillouin zone integration was carried out on

Monkhorst–Pack grids (84) with a $7 \times 7 \times 3$ k-point mesh. The crystal orbital overlap population (COOP) was calculated using the LOBSTER code. (85)

Notes

The authors declare no competing financial interest.

Acknowledgments

This work was financially supported by the National Key Research and Development Program of China (2019YFC1907805) and the Fundamental Research Funds for the Central Universities of Central South University (2021zzts0072). Moreover, the authors thank the BL11B and BL14B1 stations in the Shanghai Synchrotron Radiation Facility (SSRF) and the U19 station in the National Synchrotron Radiation Laboratory (NSRL) for XAS measurements. The authors also thank the Science Palette (Wechat: Science-Palette) and Chunlin Tan (Wechat: EditorTan) for their help with the image illustrations as well as the Shiyanjia Lab (www.shiyanjia.com) for the STEM characterization. Finally, this work was supported in part by the High Performance Computing Center of Central South University.

References

- 1 Aurbach, D.; Markovsky, B.; Salitra, G.; Markevich, E.; Talyossef, Y.; Koltypin, M.; Nazar, L.; Ellis, B.; Kovacheva, D. review on electrode-electrolyte solution interactions, related to cathode materials for Li-ion batteries. *J. Power Sources* 2007, 165, 491– 499,
- 2 Choi, N.-S.; Chen, Z.; Freunberger, S. A.; Ji, X.; Sun, Y.-K.; Amine, K.; Yushin, G.; Nazar, L. F.; Cho, J.; Bruce, P. G. Challenges facing lithium batteries and electrical double-layer capacitors. *Angew. Chem., Int. Ed.* 2012, 51, 9994– 10024,
- 3 Kraytsberg, A.; Ein-Eli, Y. Higher, stronger, better a review of 5 volt cathode materials for advanced lithium-ion batteries. *Adv. Energy Mater.* 2012, 2, 922– 939,
- 4 Whittingham, M. S. Lithium batteries and cathode materials. *Chem. Rev.* 2004, 104, 4271– 4302,
- 5 Masquelier, C.; Croguennec, L. Polyanionic (Phosphates, Silicates, Sulfates) Frameworks as electrode materials for rechargeable Li (or Na) batteries. *Chem. Rev.* 2013, 113, 6552– 6591,
- 6 Ji, Y.-R.; Weng, S.-T.; Li, X.-Y.; Zhang, Q.-H.; Gu, L. Atomic-scale structural evolution of electrode materials in Li-ion batteries: A review. *Rare Met.* 2020, 39, 205– 217,
- 7 Noh, H.-J.; Youn, S.; Yoon, C. S.; Sun, Y.-K. Comparison of the structural and electrochemical properties of layered $\text{Li}[\text{Ni}_x\text{Co}_y\text{Mn}_z]\text{O}_2$ ($x = 1/3, 0.5, 0.6, 0.7, 0.8$ and 0.85) cathode material for lithium-ion batteries. *J. Power Sources* 2013, 233, 121– 130,
- 8 Yoon, C. S.; Ryu, H.-H.; Park, G.-T.; Kim, J.-H.; Kim, K.-H.; Sun, Y.-K. Extracting maximum capacity from Ni-rich $\text{Li}[\text{Ni}_{0.95}\text{Co}_{0.025}\text{Mn}_{0.025}]\text{O}_2$ cathodes for high-energy-density lithium-ion batteries. *J. Mater. Chem. A* 2018, 6, 4126– 4132,
- 9 Kim, J.-H.; Ryu, H.-H.; Kim, S. J.; Yoon, C. S.; Sun, Y.-K. Degradation mechanism of highly Ni-rich $\text{Li}[\text{Ni}_x\text{Co}_y\text{Mn}_{1-x-y}]\text{O}_2$ cathodes with $x > 0.9$. *ACS Appl. Mater. Interfaces* 2019, 11, 30936– 30942,
- 10 Yoon, M.; Dong, Y.; Hwang, J.; Sung, J.; Cha, H.; Ahn, K.; Huang, Y.; Kang, S. J.; Li, J.; Cho, J. Reactive boride infusion stabilizes Ni-rich cathodes for lithium-ion batteries. *Nat. Energy* 2021, 6, 362,
- 11 Kim, J.-H.; Park, K.-J.; Kim, S. J.; Yoon, C. S.; Sun, Y.-K. A method of increasing the energy density of layered Ni-rich $\text{Li}[\text{Ni}_{1-2x}\text{Co}_x\text{Mn}_x]\text{O}_2$ cathodes ($x = 0.05, 0.1, 0.2$). *J. Mater. Chem. A* 2019, 7, 2694– 2701,
- 12 Kim, U. H.; Ryu, H. H.; Kim, J. H.; Mücke, R.; Kaghazchi, P.; Yoon, C. S.; Sun, Y. K. Microstructure-controlled Ni-Rich cathode material by microscale compositional partition for next-generation electric vehicles. *Adv. Energy Mater.* 2019, 9, 1803902,

- 13 Besli, M. M.; Xia, S.; Kuppan, S.; Huang, Y.; Metzger, M.; Shukla, A. K.; Schneider, G.; Hellstrom, S.; Christensen, J.; Doeff, M. M.; Liu, Y. Mesoscale chemomechanical interplay of the $\text{LiNi}_0.8\text{Co}_0.15\text{Al}_0.05\text{O}_2$ cathode in solid-state polymer batteries. *Chem. Mater.* 2018, 31, 491– 501,
- 14 Li, S.; Jiang, Z.; Han, J.; Xu, Z.; Wang, C.; Huang, H.; Yu, C.; Lee, S.-J.; Pianetta, P.; Ohldag, H.; Qiu, J.; Lee, J.-S.; Lin, F.; Zhao, K.; Liu, Y. Mutual modulation between surface chemistry and bulk microstructure within secondary particles of nickel-rich layered oxides. *Nat. Commun.* 2020, 11, 4433,
- 15 Ryu, H. H.; Park, K. J.; Yoon, D. R.; Aishova, A.; Yoon, C. S.; Sun, Y. K. $\text{Li}[\text{Ni}_0.9\text{Co}_0.09\text{W}_0.01]\text{O}_2$: A new type of layered oxide cathode with high cycling stability. *Adv. Energy Mater.* 2019, 9, 1902698,
- 16 Yoon, C. S.; Choi, M.-J.; Jun, D.-W.; Zhang, Q.; Kaghazchi, P.; Kim, K.-H.; Sun, Y.-K. cation ordering of Zr-doped LiNiO_2 cathode for lithium-ion batteries. *Chem. Mater.* 2018, 30, 1808– 1814,
- 17 Duan, J.; Wu, C.; Cao, Y.; Huang, D.; Du, K.; Peng, Z.; Hu, G. Enhanced compacting density and cycling performance of Ni-riched electrode via building mono dispersed micron scaled morphology. *J. Alloys Compd.* 2017, 695, 91– 99,
- 18 Xu, G.-L.; Liu, Q.; Lau, K. K. S.; Liu, Y.; Liu, X.; Gao, H.; Zhou, X.; Zhuang, M.; Ren, Y.; Li, J.; Shao, M.; Ouyang, M.; Pan, F.; Chen, Z.; Amine, K.; Chen, G. Building ultraconformal protective layers on both secondary and primary particles of layered lithium transition metal oxide cathodes. *Nat. Energy* 2019, 4, 484– 494,
- 19 Lee, W.; Lee, S.; Lee, E.; Choi, M.; Thangavel, R.; Lee, Y.; Yoon, W.-S. Destabilization of the surface structure of Ni-rich layered materials by water-washing process. *Energy Storage Mater.* 2022, 44, 441– 451,
- 20 Li, L.; Xu, M.; Yao, Q.; Chen, Z.; Song, L.; Zhang, Z.; Gao, C.; Wang, P.; Yu, Z.; Lai, Y. Alleviating surface degradation of nickel-rich layered oxide cathode material by encapsulating with nanoscale Li-ions/electrons superionic conductors hybrid membrane for advanced Li-ion batteries. *ACS Appl. Mater. Interfaces* 2016, 8, 30879– 30889,
- 21 Meng, K.; Wang, Z.; Guo, H.; Li, X.; Wang, D. Improving the cycling performance of $\text{LiNi}_0.8\text{Co}_0.1\text{Mn}_0.1\text{O}_2$ by surface coating with Li_2TiO_3 . *Electrochim. Acta* 2016, 211, 822– 831,
- 22 Xu, Y.-D.; Xiang, W.; Wu, Z.-G.; Xu, C.-L.; Li, Y.-C.; Guo, X.-D.; Lv, G.-P.; Peng, X.; Zhong, B.-H. Improving cycling performance and rate capability of Ni-rich $\text{LiNi}_0.8\text{Co}_0.1\text{Mn}_0.1\text{O}_2$ cathode materials by $\text{Li}_4\text{Ti}_5\text{O}_{12}$ coating. *Electrochim. Acta* 2018, 268, 358– 365,
- 23 Liang, H.; Wang, Z.; Guo, H.; Wang, J.; Leng, J. Improvement in the electrochemical performance of $\text{LiNi}_0.8\text{Co}_0.1\text{Mn}_0.1\text{O}_2$ cathode material by Li_2ZrO_3 coating. *Appl. Surf. Sci.* 2017, 423, 1045– 1053,

- 24 Zhao, E.; Chen, M.; Hu, Z.; Chen, D.; Yang, L.; Xiao, X. Improved cycle stability of high-capacity Ni-rich $\text{LiNi}_{0.8}\text{Mn}_{0.1}\text{Co}_{0.1}\text{O}_2$ at high cut-off voltage by Li_2SiO_3 coating. *J. Power Sources* 2017, 343, 345–353,
- 25 Zhang, B.; Dong, P.; Tong, H.; Yao, Y.; Zheng, J.; Yu, W.; Zhang, J.; Chu, D. Enhanced electrochemical performance of $\text{LiNi}_{0.8}\text{Co}_{0.1}\text{Mn}_{0.1}\text{O}_2$ with lithium-reactive Li_3VO_4 coating. *J. Alloys Compd.* 2017, 706, 198–204,
- 26 Yan, P.; Zheng, J.; Liu, J.; Wang, B.; Cheng, X.; Zhang, Y.; Sun, X.; Wang, C.; Zhang, J.-G. Tailoring grain boundary structures and chemistry of Ni-rich layered cathodes for enhanced cycle stability of lithium-ion batteries. *Nat. Energy* 2018, 3, 600–605,
- 27 Kim, U.-H.; Park, G.-T.; Son, B.-K.; Nam, G. W.; Liu, J.; Kuo, L.-Y.; Kaghazchi, P.; Yoon, C. S.; Sun, Y.-K. Heuristic solution for achieving long-term cycle stability for Ni-rich layered cathodes at full depth of discharge. *Nat. Energy* 2020, 5, 860–869,
- 28 Sun, H. H.; Ryu, H.-H.; Kim, U.-H.; Weeks, J. A.; Heller, A.; Sun, Y.-K.; Mullins, C. B. Beyond doping and coating: prospective strategies for stable high-capacity layered Ni-rich cathodes. *ACS Energy Lett.* 2020, 5, 1136–1146,
- 29 Liu, R.; Chen, H.; Zhao, K.; Qin, Y.; Jiang, B.; Zhang, T.; Sha, G.; Shi, X.; Uher, C.; Zhang, W.; Chen, L. Entropy as a gene-like performance indicator promoting thermoelectric materials. *Adv. Mater.* 2017, 29, 1702712,
- 30 Kim, U.-H.; Lee, E.-J.; Yoon, C. S.; Myung, S.-T.; Sun, Y.-K. Compositionally graded cathode material with long-term cycling stability for electric vehicles application. *Adv. Energy Mater.* 2016, 6, 1601417, DOI: 10.1002/aenm.201601417 [Crossref], Google ScholarOpenURL MANCHESTER METROPOLITAN UNIV
- 31 Chen, J.; Zou, G.; Deng, W.; Huang, Z.; Gao, X.; Liu, C.; Yin, S.; Liu, H.; Deng, X.; Tian, Y.; Li, J.; Wang, C.; Wang, D.; Wu, H.; Yang, L.; Hou, H.; Ji, X. Pseudo-bonding and electric-field harmony for Li-rich Mn-based oxide cathode. *Adv. Funct. Mater.* 2020, 30, 2004302,
- 32 Yu, F.-D.; Que, L.-F.; Xu, C.-Y.; Wang, M.-J.; Sun, G.; Duh, J.-G.; Wang, Z.-B. Dual conductive surface engineering of Li-rich oxides cathode for superior high-energy-density Li-ion batteries. *Nano Energy* 2019, 59, 527–536,
- 33 Wang, Y.; Wang, L.; Zhu, H.; Chu, J.; Fang, Y.; Wu, L.; Huang, L.; Ren, Y.; Sun, C. J.; Liu, Q.; Ai, X.; Yang, H.; Cao, Y. Ultralow-strain Zn-substituted layered oxide cathode with suppressed $\text{P}2\text{-O}2$ transition for stable sodium ion storage. *Adv. Funct. Mater.* 2020, 30, 1910327,

- 34 Wei, H.-x.; Tang, L.-b.; Huang, Y.-d.; Wang, Z.-y.; Luo, Y.-h.; He, Z.-j.; Yan, C.; Mao, J.; Dai, K.-h.; Zheng, J.-c. Comprehensive understanding of Li/Ni intermixing in layered transition metal oxides. *Mater. Today* 2021, 51, 365– 392,
- 35 Kong, F.; Liang, C.; Longo, R. C.; Yeon, D.-H.; Zheng, Y.; Park, J.-H.; Doo, S.-G.; Cho, K. Conflicting roles of anion doping on the electrochemical performance of Li-ion battery cathode materials. *Chem. Mater.* 2016, 28, 6942– 6952,
- 36 Yang, W.; Xiang, W.; Chen, Y.-X.; Wu, Z.-G.; Hua, W.-B.; Qiu, L.; He, F.-R.; Zhang, J.; Zhong, B.-H.; Guo, X.-D. Interfacial regulation of Ni-rich cathode materials with an ion-conductive and pillaring layer by infusing gradient boron for improved cycle stability. *ACS Appl. Mater. Interfaces* 2020, 12, 10240– 10251,
- 37 Liu, Y.; Wang, J.; Wu, J.; Ding, Z.; Yao, P.; Zhang, S.; Chen, Y. 3D cube-maze-like Li-rich layered cathodes assembled from 2D porous nanosheets for enhanced cycle stability and rate capability of lithium-ion batteries. *Adv. Energy Mater.* 2019, 10, 1903139,
- 38 Wu, B.; Lu, W. Mechanical modeling of particles with active core-shell structures for lithium-ion battery electrodes. *J. Phys. Chem. C* 2017, 121, 19022– 19030
- 39 Xin, F.; Zhou, H.; Zong, Y.; Zuba, M.; Chen, Y.; Chernova, N. A.; Bai, J.; Pei, B.; Goel, A.; Rana, J.; Wang, F.; An, K.; Piper, L. F. J.; Zhou, G.; Whittingham, M. S. What is the role of Nb in nickel-rich layered oxide cathodes for lithium-ion batteries?. *ACS Energy Lett.* 2021, 6, 1377– 1382,
- 40 Zhu, Y.; Sun, W.; Luo, J.; Chen, W.; Cao, T.; Zheng, L.; Dong, J.; Zhang, J.; Zhang, M.; Han, Y.; Chen, C.; Peng, Q.; Wang, D.; Li, Y. A cocoon silk chemistry strategy to ultrathin N-doped carbon nanosheet with metal single-site catalysts. *Nat. Commun.* 2018, 9, 3861,
- 41 Ryu, H.-H.; Park, G.-T.; Yoon, C. S.; Sun, Y.-K. Suppressing detrimental phase transitions via tungsten doping of LiNiO₂ cathode for next-generation lithium-ion batteries. *J. Mater. Chem. A* 2019, 7, 18580– 18588,
- 42 Ryu, H.-H.; Park, K.-J.; Yoon, C. S.; Sun, Y.-K. Capacity fading of ni-rich Li[Ni_xCo_yMn_{1-x-y}]O₂ (0.6 ≤ x ≤ 0.95) cathodes for high-energy-density lithium-ion batteries: bulk or surface degradation?. *Chem. Mater.* 2018, 30, 1155– 1163,
- 43 Ryu, H.-H.; Park, N.-Y.; Seo, J. H.; Yu, Y.-S.; Sharma, M.; Mücke, R.; Kaghazchi, P.; Yoon, C. S.; Sun, Y.-K. A highly stabilized Ni-rich NCA cathode for high-energy lithium-ion batteries. *Mater. Today* 2020, 36, 73– 82,

- 44 Yoon, C. S.; Jun, D.-W.; Myung, S.-T.; Sun, Y.-K. structural stability of LiNiO₂ cycled above 4.2 V. *ACS Energy Lett.* 2017, 2, 1150– 1155,
- 45 Aishova, A.; Park, G. T.; Yoon, C. S.; Sun, Y. K. Cobalt-free high-capacity Ni-rich layered Li[Ni_{0.9}Mn_{0.1}]O₂ cathode. *Adv. Energy Mater.* 2019, 10, 1903179,
- 46 Kim, U.-H.; Myung, S.-T.; Yoon, C. S.; Sun, Y.-K. Extending the battery life using an Al-doped Li[Ni_{0.76}Co_{0.09}Mn_{0.15}]O₂ cathode with concentration gradients for lithium ion batteries. *ACS Energy Lett.* 2017, 2, 1848– 1854,
- 47 Wang, P.; Liu, P.-A.; Ye, S. Preparation and microwave absorption properties of Ni(Co/Zn/Cu)Fe₂O₄/SiC@SiO₂ composites. *Rare Met.* 2019, 38, 59– 63,
- 48 Yin, S.; Deng, W.; Chen, J.; Gao, X.; Zou, G.; Hou, H.; Ji, X. Fundamental and solutions of microcrack in Ni-rich layered oxide cathode materials of lithium-ion batteries. *Nano Energy* 2021, 83, 105854,
- 49 Kondrakov, A. O.; Geßwein, H.; Galdina, K.; de Biasi, L.; Meded, V.; Filatova, E. O.; Schumacher, G.; Wenzel, W.; Hartmann, P.; Brezesinski, T.; Janek, J. Charge-transfer-induced lattice collapse in Ni-rich NCM cathode materials during delithiation. *J. Phys. Chem. C* 2017, 121, 24381– 24388,
- 50 Yang, W.; Qiao, R. Soft X-ray Spectroscopy for probing electronic and chemical states of battery materials. *Chin. Phys. B* 2016, 25, 017104,
- 51 Qiao, R.; Wray, L. A.; Kim, J.-H.; Pieczonka, N. P. W.; Harris, S. J.; Yang, W. Direct experimental probe of the Ni(II)/Ni(III)/Ni(IV) redox evolution in LiNi_{0.5}Mn_{1.5}O₄ electrodes. *J. Phys. Chem. C* 2015, 119, 27228– 27233,
- 52 Farges, F. Ab initio and experimental Pre-edge investigations of the Mn K-edge XANES in oxide-type materials. *Phys. Rev. B: Condens. Matter Mater. Phys.* 2005, 71, 155109,
- 53 Tsai, Y. W.; Hwang, B. J.; Ceder, G.; Sheu, H. S.; Liu, D. G.; Lee, J. F. In-situ X-ray absorption spectroscopic study on variation of electronic transitions and local structure of LiNi_{1/3}Co_{1/3}Mn_{1/3}O₂ cathode material during electrochemical cycling. *Chem. Mater.* 2005, 17, 3191– 3199
- 54 Sharpe, R.; House, R. A.; Clarke, M. J.; Förstermann, D.; Marie, J.-J.; Cibir, G.; Zhou, K.-J.; Playford, H. Y.; Bruce, P. G.; Islam, M. S. Redox chemistry and the role of trapped molecular O₂ in Li-rich disordered rocksalt oxyfluoride cathodes. *J. Am. Chem. Soc.* 2020, 142, 21799– 21809,
- 55 Liu, Y.; Zhu, H.; Zhu, H.; Ren, Y.; Zhu, Y.; Huang, Y.; Dai, L.; Dou, S.; Xu, J.; Sun, C. J.; Wang, X. L.; Deng, Y.; Yuan, Q.; Liu, X.; Wu, J.; Chen, Y.; Liu, Q. Modulating the surface ligand orientation for stabilized anionic redox in Li-rich oxide cathodes. *Adv. Energy Mater.* 2021, 11, 2003479,

- 56 Hu, G.; Tao, Y.; Lu, Y.; Fan, J.; Li, L.; Xia, J.; Huang, Y.; Zhang, Z.; Su, H.; Cao, Y. Enhanced electrochemical properties of $\text{LiNi}_0.8\text{Co}_0.1\text{Mn}_0.1\text{O}_2$ cathode materials modified with lithium-ion conductive coating LiNbO_3 . *ChemElectroChem* 2019, 6, 4773–4780,
- 57 Dai, Y.-Q.; Li, G.-C.; Li, X.-H.; Guo, H.-J.; Wang, Z.-X.; Yan, G.-C.; Wang, J.-X. Ultrathin porous graphitic carbon nanosheets activated by alkali metal salts for high power density lithium-ion capacitors. *Rare Met.* 2020, 39, 1364–1373,
- 58 Zhao, W.; Zheng, J.; Zou, L.; Jia, H.; Liu, B.; Wang, H.; Engelhard, M. H.; Wang, C.; Xu, W.; Yang, Y.; Zhang, J. G. High voltage operation of Ni-rich NMC cathodes enabled by stable electrode/electrolyte interphases. *Adv. Energy Mater.* 2018, 8, 1800297,
- 59 Yang, L.; Ravdel, B.; Lucht, B. L. Electrolyte reactions with the surface of high voltage $\text{LiNi}_0.5\text{Mn}_1.5\text{O}_4$ cathodes for lithium-ion batteries. *Electrochem. Solid-State Lett.* 2010, 13, A95–A97,
- 60 Zheng, J.; Yan, P.; Mei, D.; Engelhard, M. H.; Cartmell, S. S.; Polzin, B. J.; Wang, C.; Zhang, J. G.; Xu, W. Highly stable operation of lithium metal batteries enabled by the formation of a transient high-concentration electrolyte layer. *Adv. Energy Mater.* 2016, 6, 1502151
- 61 Park, S.; Jeong, S. Y.; Lee, T. K.; Park, M. W.; Lim, H. Y.; Sung, J.; Cho, J.; Kwak, S. K.; Hong, S. Y.; Choi, N.-S. Replacing conventional battery electrolyte additives with dioxolone derivatives for high-energy-density lithium-ion batteries. *Nat. Commun.* 2021, 12, 838,
- 62 Myung, S.-T.; Maglia, F.; Park, K.-J.; Yoon, C. S.; Lamp, P.; Kim, S.-J.; Sun, Y.-K. Nickel-rich layered cathode materials for automotive lithium-ion batteries: achievements and perspectives. *ACS Energy Lett.* 2016, 2, 196–223,
- 63 Eum, D.; Kim, B.; Kim, S. J.; Park, H.; Wu, J.; Cho, S.-P.; Yoon, G.; Lee, M. H.; Jung, S.-K.; Yang, W.; Seong, W. M.; Ku, K.; Tamwattana, O.; Park, S. K.; Hwang, I.; Kang, K. Voltage decay and redox asymmetry mitigation by reversible cation migration in lithium-rich layered oxide electrodes. *Nat. Mater.* 2020, 19, 419–427,
- 64 Ge, P.; Li, S.; Xu, L.; Zou, K.; Gao, X.; Cao, X.; Zou, G.; Hou, H.; Ji, X. Hierarchical hollow-microsphere metal-selenide@carbon composites with rational surface engineering for advanced sodium storage. *Adv. Energy Mater.* 2019, 9, 1803035,
- 65 Ge, P.; Li, S.; Shuai, H.; Xu, W.; Tian, Y.; Yang, L.; Zou, G.; Hou, H.; Ji, X. Ultrafast sodium full batteries derived from XFe ($\text{X} = \text{Co}, \text{Ni}, \text{Mn}$) prussian blue analogs. *Adv. Mater.* 2019, 31, e1806092
- 66 Ben Yahia, M.; Vergnet, J.; Saubanère, M.; Doublet, M.-L. Unified picture of anionic redox in Li/Na-ion batteries. *Nat. Mater.* 2019, 18, 496–502,

- 67 Krasnikova, I. V.; Pogosova, M. A.; Sanin, A. O.; Stevenson, K. J. Toward standardization of electrochemical impedance spectroscopy studies of Li-ion conductive ceramics. *Chem. Mater.* 2020, 32, 2232– 2241,
- 68 Bredar, A. R. C.; Chown, A. L.; Burton, A. R.; Farnum, B. H. Electrochemical impedance spectroscopy of metal oxide electrodes for energy applications. *ACS Appl. Energy Mater.* 2020, 3, 66– 98,
- 69 Wu, F.; Liu, J.; Li, L.; Zhang, X.; Luo, R.; Ye, Y.; Chen, R. Surface modification of Li-Rich cathode materials for lithium-ion batteries with a PEDOT: PSS conducting polymer. *ACS Appl. Mater. Interfaces* 2016, 8, 23095– 23104,
- 70 Wang, Y.-Y.; Sun, Y.-Y.; Liu, S.; Li, G.-R.; Gao, X.-P. Na-doped $\text{LiNi}_{0.8}\text{Co}_{0.15}\text{Al}_{0.05}\text{O}_2$ with excellent stability of both capacity and potential as cathode materials for Li-ion batteries. *ACS Appl. Energy Mater.* 2018, 1, 3881– 3889,
- 71 Ohta, N.; Takada, K.; Sakaguchi, I.; Zhang, L.; Ma, R.; Fukuda, K.; Osada, M.; Sasaki, T. LiNbO_3 -coated LiCoO_2 as cathode material for all solid-state lithium secondary batteries. *Electrochem. Commun.* 2007, 9, 1486– 1490,
- 72 Li, G. R.; Feng, X.; Ding, Y.; Ye, S. H.; Gao, X. P. AlF_3 -coated $\text{Li}(\text{Li}_{0.17}\text{Ni}_{0.25}\text{Mn}_{0.58})\text{O}_2$ as cathode material for li-ion batteries. *Electrochim. Acta* 2012, 78, 308– 315,
- 73 Zhang, W.; Sun, X.; Tang, Y.; Xia, H.; Zeng, Y.; Qiao, L.; Zhu, Z.; Lv, Z.; Zhang, Y.; Ge, X.; Xi, S.; Wang, Z.; Du, Y.; Chen, X. Lowering charge transfer barrier of LiMn_2O_4 via nickel surface doping to enhance Li^+ intercalation kinetics at subzero temperatures. *J. Am. Chem. Soc.* 2019, 141, 14038,
- 74 Jiang, W.; Yin, C.; Xia, Y.; Qiu, B.; Guo, H.; Cui, H.; Hu, F.; Liu, Z. Understanding the discrepancy of defect kinetics on anionic redox in lithium-rich cathode oxides. *ACS Appl. Mater. Interfaces* 2019, 11, 14023– 14034,
- 75 Deng, S.; Wang, B.; Yuan, Y.; Li, X.; Sun, Q.; Doyle-Davis, K.; Banis, M. N.; Liang, J.; Zhao, Y.; Li, J.; Li, R.; Sham, T.-K.; Shahbazian-Yassar, R.; Wang, H.; Cai, M.; Lu, J.; Sun, X. Manipulation of an ionic and electronic conductive interface for highly-stable high-voltage cathodes. *Nano Energy* 2019, 65, 103988,
- 76 Zhou, L.; Zhao, D.; Lou, X. D. $\text{LiNi}_{0.5}\text{Mn}_{1.5}\text{O}_4$ hollow structures as high-performance cathodes for lithium-ion batteries. *Angew. Chem., Int. Ed.* 2012, 51, 239– 241,
- 77 Kohn, W.; Sham, L. J. Self-consistent equations including exchange and correlation effects. *Phys. Rev.* 1965, 140, A1133– A1138,

- 78 Hohenberg, P.; Kohn, W. Inhomogeneous electron gas. *Phys. Rev.* 1964, 136, B864– B871,
- 79 Kresse, G.; Furthmüller, J. Efficient iterative schemes for ab initio total-energy calculations using a plane-wave basis set. *Phys. Rev. B: Condens. Matter Mater. Phys.* 1996, 54, 11169– 11186,
- 80 Blöchl, P. E. Projector augmented-wave method. *Phys. Rev. B: Condens. Matter Mater. Phys.* 1994, 50, 17953– 17979,
- 81 Perdew, J. P.; Burke, K.; Ernzerhof, M. Perdew, burke, and ernzerhof reply. *Phys. Rev. Lett.* 1998, 80, 891,
- 82 Yang, H.; Wu, H. H.; Ge, M.; Li, L.; Yuan, Y.; Yao, Q.; Chen, J.; Xia, L.; Zheng, J.; Chen, Z.; Duan, J.; Kisslinger, K.; Zeng, X. C.; Lee, W. K.; Zhang, Q.; Lu, J. Simultaneously dual modification of Ni-rich layered oxide cathode for high-energy lithium-ion batteries. *Adv. Funct. Mater.* 2019, 29, 1808825,
- 83 Ceperley, D. M.; Alder, B. J. Ground state of the electron gas by a stochastic method. *Phys. Rev. Lett.* 1980, 45, 566– 569,
- 84 Monkhorst, H. J.; Pack, J. D. Special points for Brillouin-zone integrations. *Phys. Rev. B: Solid State* 1976, 13, 5188– 5192,
- 85 Dronskowski, R.; Bloechl, P. E. Crystal orbital hamilton populations (COHP). Energy-resolved visualization of chemical bonding in solids based on density-functional calculations. *J. Phys. Chem.* 1993, 97, 8617– 8624,